Ceramics International 42 (2016) 17317–17331

Contents lists available at ScienceDirect

Ceramics International

journal homepage: www.elsevier.com/locate/ceramint

Microwave, dielectric and magnetic properties of Mg-Ti substituted Ni-Zn ferrite nanoparticles

B. Ünal [a], İ.S. Ünver [b], H. Güngüneş [c], U. Topal [d], A. Baykal [e], H. Sözeri [d,*]

[a] Department of Computer Engineering, Istanbul Sabahattin Zaim University, Halkali Cad. No. 2, 34303 K. Çekmece-Istanbul, Turkey
[b] Department of Physics, Gebze Technical University, 41400 Kocaeli, Turkey
[c] Department of Physics, Hitit University, Çevre Yolu Bulvarı, 19030 Çorum, Turkey
[d] TUBITAK-UME, National Metrology Institute, PO Box 54, 41470 Gebze, Kocaeli, Turkey
[e] Chemistry Department, Fatih University, 34500 B. Çekmece-Istanbul, Turkey

ARTICLE INFO

Article history:
Received 20 May 2016
Received in revised form
12 July 2016
Accepted 4 August 2016
Available online 5 August 2016

Keywords:
Spinel ferrites
Solid state reaction
Microwave properties
Magnetic measurements
Nanoparticles

ABSTRACT

Mg-Ti substituted Ni-Zn spinel ferrites ($Ni_{0.5}Zn_{0.5}Mg_xTi_xFe_{2-2x}O_4$, where $0.05 \leq x \leq 0.25$) have been prepared by conventional solid state reaction method. 1 wt% B_2O_3 was added to increase the crystal growth at low temperatures. The structural characterization of samples was performed by X-ray powder diffractometry, scanning electron microscopy and Mössbauer spectroscopy. Magnetic parameters of samples were measured by vibrating sample magnetometer at room temperature. Microwave characteristics were determined by near field measurements using a network analyzer in reflection/transmission mode. Mössbauer spectra of all the samples consist of 3 sextets and one doublet. Variation of the line width, isomer shift, quadrupole splitting and hyperfine magnetic field values have been obtained from the ^{57}Fe Mössbauer spectroscopy data for Ni-Zn spinels having different Mg^{2+} and Ti^{4+} concentrations. The saturation magnetization of the samples decreases as the concentration of Mg-Ti ions increases, which can be explained by site preferences of the substituted cations. The electrical properties of Mg-Ti substituted Ni-Zn spinel ferrites were examined extensively as a function of temperature, frequency and Mg-Ti amount. It was found that Mg-Ti substitution has a strong effect on the ac conductivity, dielectric constant and dielectric loss mechanisms. The activation energy levels can be regulated by varying Mg-Ti concentration. There is one reflection minimum observed in the microwave characterization of the samples in the 2–18 GHz range located around 10 GHz in X-band, the mechanism of which is the quarter wave cancellation due to the matching thickness. The $Ni_{0.5}Zn_{0.5}Mg_{0.2}Ti_{0.2}Fe_{1.6}O_4$ sample has the best microwave properties with the reflection loss of −29 dB at 10.4 GHz for a thickness of 3 mm and better than −35 dB at 16 GHz when thickness is decreased to 2 mm. As a result, it was concluded that this material can be used as microwave absorber both in X and Ku-bands.

1. Introduction

Microwave absorbers are functional materials having magnetic and/or dielectric fillers which convert incoming electromagnetic energy into the heat due to the resonance and relaxation of dipoles and magnetic moments. They have attracted great interest due to the advancement of wireless communication systems and EMI/EMC requirements for both industrial and military electronic devices. For practical applications, absorbing materials should have not only strong absorption and broad bandwidth, but also light weight and low thickness. Among various absorbing materials, ferrites have widespread usage due to their high chemical stability, low cost, excellent magnetic and dielectric properties [1–3]. However, at high frequencies of the order of GHz, the permittivity of ferrites is almost constant with its imaginary part (ε″) is close to 0. Consequently, the dielectric loss is almost negligible, and their absorbing performance mainly depends on the magnetic loss. On the other hand, this disadvantage can be overcome by tuning their magnetic, and thus, microwave properties by doping with various metallic ions, such as Cu, Zn, Co, Ti, Mn, Mg, Ni etc. [4,5].

Both hexaferrites and spinels have substantial magnetic losses in the vicinity of their natural resonance (FMR), thus, they are ones of the best materials as microwave absorbers. Spinel ferrites have a general formula of AB_2O_4 with the composition of Fe_2O_3-MO where M is generally a transition element. Almost any divalent transition-metal ion(s) can be used to form spinel ferrite. They have generally ferrimagnetic type ordering described by the Neel's

* Corresponding author.
E-mail address: huseyin.sozeri@tubitak.gov.tr (H. Sözeri).

http://dx.doi.org/10.1016/j.ceramint.2016.08.028
0272-8842/

two sublattice model. Among the spinel ferrites, Nickel-Zinc (Ni-Zn) spinel ferrite is widely used as a magnetic filler in microwave absorbing materials because of its high Curie temperature, high permeability, high resistivity and low hysterisis losses in the frequency range from several hundred MHz to several GHz [6].

Various preparation routes have been used to synthesize nanosize Ni-Zn ferrite powders such as high-energy ball milling [7], citrate precursor method [8], co-precipitation method [9], hydrothermal route [10], reverse micelle process [11], sol-gel method [12] and solid state reaction with B_2O_3 addition as a catalyst [13,14]. Ni-Zn ferrites were prepared in various forms such as core-shell nanoparticles [15,16], nanofibers [17–19], nanocomposites [20,21] and in a polymer matrix [22,23]. Several divalent ions such as Co^{2+} [24], Mn^{2+} [13], Mg^{2+}-La^{3+} [25], Nd^{2+} [26], Cu^{2+} [27] and Mn-Co [14] have been replaced by either transition metal or Fe^{3+} ions. Substitution of small amount of Nd^{2+} ions into the iron site, for instance, yielded a reflection loss (RL) of −20.7 dB@12 GHz in a 2 mm sample. When 20% Cu^{2+} ions were replaced by Ni and Zn ions, the minimum RL of −35.3 dB occurred at 11.7 GHz in a 3 mm thick sample and −35.6 dB was observed at 1.1 GHz in a 9.2 mm thick sample. A small amount of Mn^{2+} substitution to the Ni-Zn site gives rise to a RL of better than −20 dB@1.8 GHz in samples having 10 mm thickness. When both Mn and Co ions were introduced together into Ni-Zn sites, a minimum RL of −25 dB was observed in $Ni_{0.6}Zn_{0.2}Mn_{0.1}Co_{0.1}Fe_2O_4$ and $Ni_{0.8}Mn_{0.1}Co_{0.1}Fe_2O_4$ nanoparticles at 10 and 12 GHz, respectively, in 3 mm thick samples. It was also reported that magnetic and microwave properties of Ni-Zn ferrite were strongly influenced by the ratio of Ni and Zn [12,14,28].

In this study, Mg^{2+}-Ti^{4+} ions were replaced by Fe^{3+} ions in Ni-Zn ferrite in order to change magnetocrystalline anisotropy of the nanoparticles, which alters their magnetic and microwave properties accordingly. For this purpose, samples in the form of $Ni_{0.5}Zn_{0.5}Mg_xTi_xFe_{2-2x}O_4$, where $0.05 \leq x \leq 0.25$ were synthesized using conventional solid state reaction route with w.t. 1% B_2O_3 addition which was used as a catalyst to inhibit crystal growth. The structural, magnetic, dielectric and microwave properties of samples have been studied in detail.

2. Experimental

Mg-Ti substituted Ni-Zn ferrite samples were prepared using the conventional solid state reaction method. The initial oxides (i.e., NiO, MgO, ZnO, TiO, Fe_2O_3) were mixed with an appropriate molar ratio in an agate mortar for 15 min. 1 wt% B_2O_3 was added to this mixture to initiate crystal growth at low temperatures [29]. Then, powders were pelletized under 200 MPa pressure to have better magnetic properties and to increase the target phase fraction [30]. The sintering was carried at 1100 °C for 2 h. The particle size of the samples was reduced using ball milling at 1000 RPM for 2 h. Toroidal samples with inner and outer diameters of 3 and 7 mm were prepared to measure microwave properties up to 18 GHz in a coaxial waveguide. All samples, which were used in the microwave measurements, have the same thicknesses of 3 mm.

The structural characterization of the synthesized samples was performed using X-Ray powder diffractometer (Shimadzu-XRD6000, Cu-Kα radiation). The particle size and morphology of the powders were examined with a scanning electron microscope (JEOL 6335F, Field Emission Gun). Mössbauer spectra of the Ni-Zn spinels were recorded at room temperature with a spectrometer working in the constant acceleration mode using a 25 mCi ^{57}Co (Rh matrix) radiation source in transmission geometry. The Wissel velocity drive was used. The speed scale was calibrated using α-Fe and the velocity calibration was performed with laser interferometry. The obtained spectra were analyzed and fitted by the least square method using Win-Normos least squares fitting software. The quality of data fitting was checked by the χ^2-test. The magnetic characterization of the samples, all in powder form, was done at room temperature using a vibrating sample magnetometer (LDJ Electronics Inc., Model 9600) in an applied field of 15 kOe. A planetary ball milling device (Fritch, Premium Line 7) was used to reduce particle size with 5 mm ZrO_2 balls. Microwave measurements were performed in Reflection/Transmission mode in a coaxial airline using HP PNA E8364B vector network analyzer in the frequency range of 2–18 GHz. The material measurement software was used to derive complex permeability and permittivity values from the measured transmission (S_{21}) and reflection (S_{11}) coefficients.

3. Results and discussion

3.1. XRD analysis

Fig. 1a and b shows, respectively, XRD powder patterns with Rietveld analysis and variation of the lattice constant (a_o) with Mg^{2+}-Ti^{4+} concentration changing from x=0.05 to x=0.25 for $Ni_{0.5}Zn_{0.5}Mg_xTi_xFe_{2-2x}O_4$ nanoparticles (NPs). The diffraction patterns confirm a single spinel ferrite phase formation in all the samples. It has been observed that all the diffraction peaks for each sample can be well indexed to the standard diffraction peaks of spinel ferrites with cubic spinel structure of both $ZnFe_2O_4$ (JCPDS 22-1012) and $NiFe_2O_4$ (JCPDS 74-2081). There are almost no diffraction peaks corresponding to impurity phases, suggesting that pure products were obtained. Presence of eight diffraction planes (111), (220), (311), (222), (400), (422), (511) and (440) in the diffraction pattern confirms the formation of a cubic spinel ferrite structure.

The ionic radii of Ti^{4+}, Mg^{2+} and Fe^{3+} ions are 0.068 [31], 0.072 [32], 0.065 nm [32] respectively. Ti^{4+} has a strong tendency to enter into B sublattices [33]. As reported earlier, Mg^{2+} ions have a strong preference to occupy B sites and partially occupy A sites [34]. Due to the larger ionic radius of the doping ions (Mg^{2+} and Ti^{4+}), the lattice parameter "a_o" of the synthesized Ni-Zn ferrites increases (Fig. 1b). The average crystallite sizes of the samples were calculated from X-ray line broadening of the reflection using Scherrer's equation ($D=0.89\lambda/(\beta^* \mathrm{Cos}\ \theta)$), where λ is the wavelength of the X-ray radiation, θ is the diffraction angle and β is the full width at half maximum (FWHM), and were found to be within the range of 19–27 nm (Table 1).

3.2. SEM analysis

SEM micrographs of the $Ni_{0.5}Zn_{0.5}Mg_xTi_xFe_{2-2x}O_4$ spinel ferrite samples are shown in Fig. 2. The morphology and average grain size exhibit some differences for each sample as Mg-Ti concentration changes from x=0.05 to 0.25. In general, particles have well-defined grain boundaries and agglomeration is less significant with increasing Mg-Ti amount. An inhomogenous particle size distribution varying between 1 and 2 μm was observed. This can cause interaction of particles with incoming microwave in a wide wavelength range, which consequently results in having reflection losses in a wide frequency band that is desired for an ideal absorber.

3.3. Mössbauer spectroscopy

^{57}Fe Mössbauer spectra of spinel ferrite system, $Ni_{0.5}Zn_{0.5}Mg_xTi_xFe_{2-2x}O_4$; x: 0, 0.05, 0.1, 0.15 and 0.2 were recorded at room temperature and are shown in Fig. 3. Mössbauer

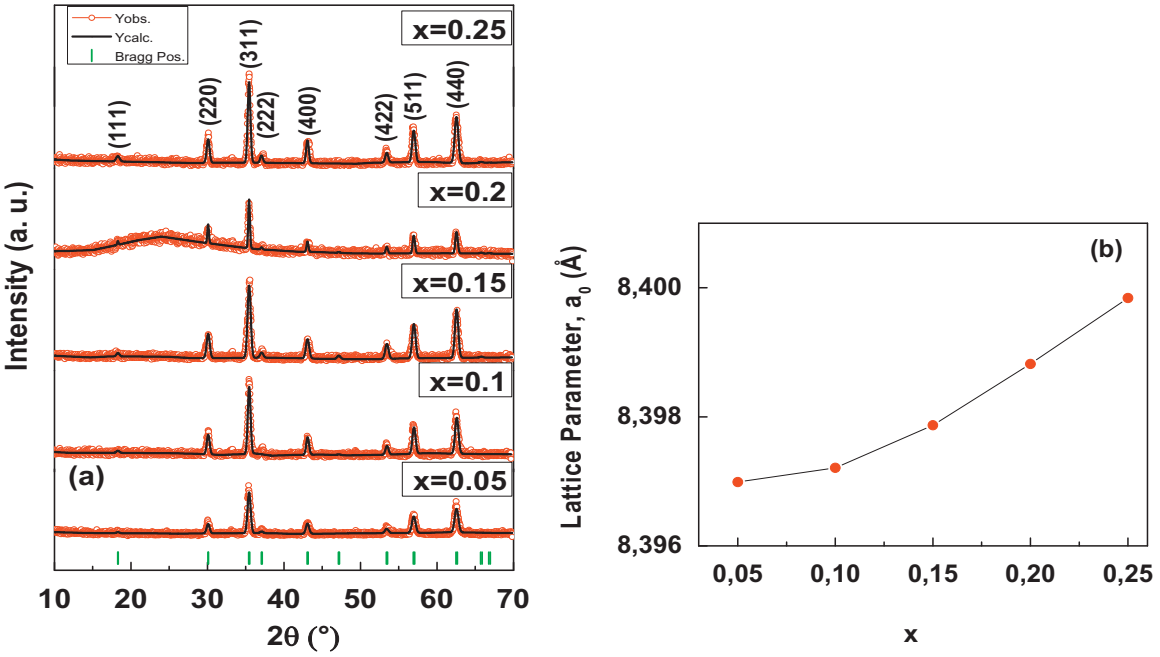

Fig. 1. (a) XRD profile fits for $Zn_{0.5}Ni_{0.5}Mg_xTi_xFe_{2-2x}O_4$ NPs, (b) Lattice parameters according to the variation of x.

Table 1
Crystalitte sizes of $Ni_{0.5}$ $Zn_{0.5}Mg_xTi_xFe_{2-2x}O_4$ NPs calculated by Scherrer's formula from the (114) peak.

x	D (nm)
0.05	19.04
0.10	22.99
0.15	20.28
0.20	27.29
0.25	21.51

spectroscopy is a highly sensitive tool to detect changes in the atomic configuration surrounding Fe ions. Various Mössbauer parameters calculated from the fitting of the spectra are given in Table 2. Each spectrum exhibits a superposition of three Zeeman sextets and one paramagnetic doublet. The largest hyperfine field with bigger isomer shift is characteristic of Fe^{3+} ions in the octahedral B-site, whereas the lower values of both parameters are due to Fe^{3+} ions in the tetrahedral A site [35–37]. The B-site subspectra were found to be composed of two sextets, B and B_1 associated with Fe^{3+} ions at two different environments in B-site [38]. The existence of the paramagnetic phase in the Mössbauer spectra may be due to the fact that a fraction of Fe ions have few nearest neighbors which probably have ordered spins, but the existence of the six-line magnetic pattern is due to the super exchange interaction between the magnetic ions at A– and B–sublattices. The paramagnetic doublet might also be arising from fine superparamagnetic grains of ferrites.

The chemical isomer shift occurs due to the change in nuclear radius and differing chemical environments. The isomer shift for A sites is less than that of B sites, because of higher covalence (i.e., larger overlapping of Fe^{3+}–O^{2-} ions at A sites when compared to B sites) [39]. The observed range of the isomer shift of the A and B magnetic patterns is 0.2781–0.3919 mms^{-1} at room temperature. It is well known that in the magnetically ordered phase, the valence of Fe can be determined by the isomer shift (0.6–1.7 mms^{-1} for Fe^{2+}, 0.05–0.5 mms^{-1} for Fe^{3+} and −0.15–0.05 mms^{-1} for Fe^{4+}) [40]. Therefore, the isomer shift values correspond to characteristics of the Fe^{3+} charge state in A and B sites. It is observed that the magnitude of the isomer shift of the A site increases very slightly with increasing concentrations of Mg^{2+} and Ti^{4+} ions. But the isomer shift of the other sites shows no appreciable change. This shows that the s-electron density around the Fe^{3+} nucleus at the A site decreases, but other sublattices are largely unaffected while Mg^{2+}- Ti^{4+} concentration increases.

The value of Q.S can provide information about the symmetry of crystal lattice and its local distortions. Both the effective charge on the neighboring ions and nonspherical distribution of 3d electrons of the cation cause an electric field gradient (EFG) [41]. The values of Q.S for observed components having various Mg-Ti amounts are negligible. This is attributed to the fact that overall cubic symmetry is maintained between Fe^{3+} ions and their surrounding which includes the substituted ions.

Variation of the hyperfine magnetic field of different sextets as a function of Mg^{2+} and Ti^{4+} substitution is given in Fig. 4, which shows that the hyperfine field values at A, B and B_1 sites decrease gradually with increasing Mg^{2+} and Ti^{4+} ion concentration (x). The distribution of Fe ion over A- and B- sites is proportional to the relative area of A- and B- Mössbauer sub-spectra. As shown in Table 2**,** the relative area of A sites increases with the addition of Mg^{2+} and Ti^{4+} ions. This shows that the non-magnetic Mg^{2+} and Ti^{4+} ions prefer to be at B-site. Replacement of Mg^{2+} and Ti^{4+} ions (0 μ_B) by the Fe^{3+} cation (5 μ_B) at octahedral B-site, which causes a reduction in the number of active linkages between A and B sites, reduces thereby the hyperfine magnetic field at both the sublattices.

3.4. Magnetic properties

Magnetic properties of the synthesized Ni-Zn ferrites have been determined by measuring M-H hysterisis curves at room temperature. Saturation magnetization values were determined from the intersection of hysterisis curves with the 1/H axis as 1/H approaches zero. Fig. 5 shows that the highest saturation magnetization occurs in the sample having the minimum Mg-Ti

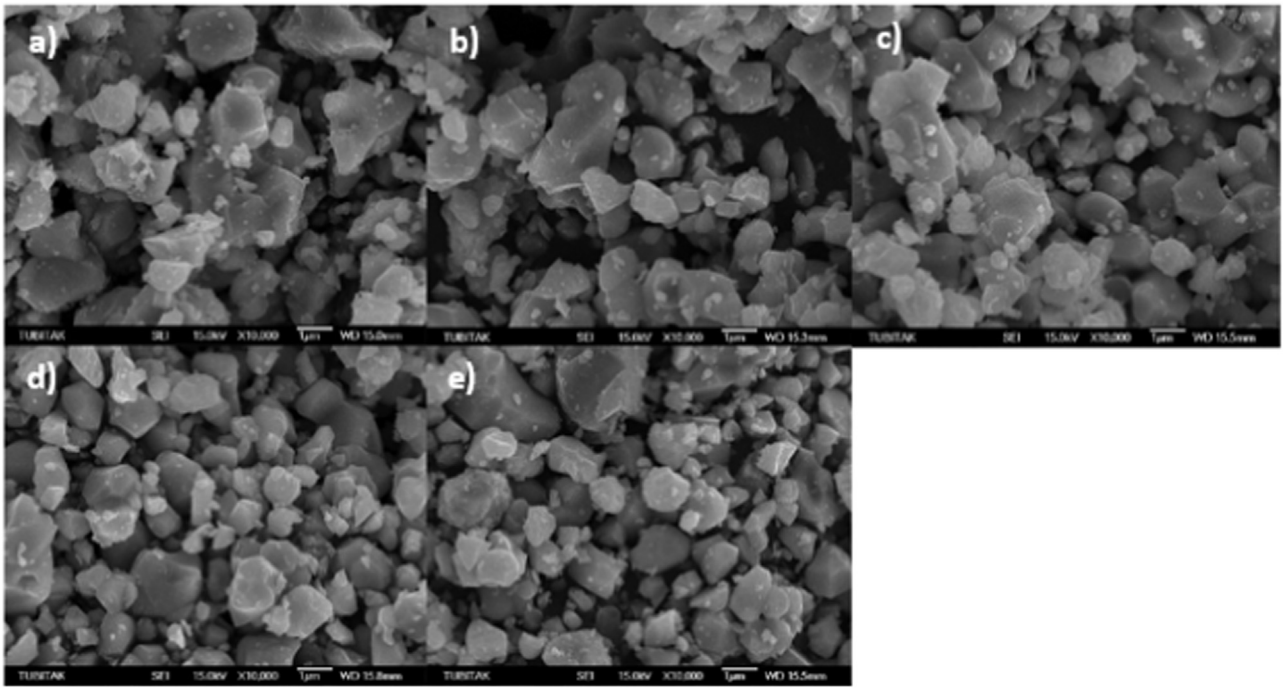

Fig. 2. SEM micrographs of a) $Ni_{0.5}Zn_{0.5}Mg_{0.05}Ti_{0.05}Fe_{1.90}O_4$ b) $Ni_{0.5}Zn_{0.5}Mg_{0.10}Ti_{0.10}Fe_{1.8}O_4$ c) $Ni_{0.5}Zn_{0.5}Mg_{0.15}Ti_{0.15}Fe_{1.7}O_4$ d) $Ni_{0.5}Zn_{0.5}Mg_{0.20}Ti_{0.02}Fe_{1.6}O_4$ e) $Ni_{0.5}Zn_{0.5}Mg_{0.25}Ti_{0.25}Fe_{1.5}O_4$ NPs.

concentration (x=0.05) with Ms value of 33.4 emu/g. In addition, the sample with the highest Mg-Ti concentration has the lowest saturation magnetization of 17.7 emu/g. This decrease in the saturation magnetization with increasing Mg-Ti concentration can be explained by site preferences of Mg^{2+} and Ti^{4+} ions and the strength of the exchange interactions. Ni-Zn ferrite has a mixed spinel structure with a general formula of $\left[Fe^{3+}_{1-x}Zn^{2+}_{x}\right]^{A}\left[Ni^{2+}_{1-x}Fe^{3+}_{1+x}\right]^{B}O_4$, where A represents tetrahedral and B denotes octahedral sites. Magnetization of the spinels has been explained by Neel's two sub-lattice model of ferrimagnetism [42]. According to this model, magnetic moments in A- and B-sublattices are aligned antiparallel to each other and their spins have a collinear structure. Thus, total magnetization can be found as $M=|M_B-M_A|$. The non-magnetic Mg^{2+} and Ti^{4+} ions were replaced by Fe^{3+} ions having magnetic moment of 5 μB at B-site, which in turn decreases the magnetization of the B-sublattice. Thus, total magnetization of the samples decreases. In addition, there are three types of exchange interactions between A and B-sites, as J_{AA} (inter A-site), J_{AB} (between A and B sites) and J_{BB} (inter B-side). Among these, antiferromagnetic super exchange interaction J_{AB}, which takes place between Fe^{3+} ions in different sites over oxygen ions (i.e., $Fe^{3+}_{site-A} - O^{2+} - Fe^{3+}_{site-B}$), is the strongest one. As the number of Fe^{3+} ions in B-sites decreases, J_{AB} super exchange interaction weakens, and hence, the net magnetization of the samples decreases. Magnetic parameters of all samples are presented in Table 3.

Like saturation magnetization, the coercivity of Ni-Zn ferrites decreases almost linearly with increasing Mg-Ti concentration. The coercivity depends on the magnetocrystalline anisotropy, particle size and saturation magnetization of particles and can be expressed as; $H_c = \frac{2K_1}{\mu_0 M_s}$. The magnetocrystalline anisotropy of the samples is a sum of bulk and surface anisotropies which are related by the equation $K_{eff}=K_{bulk}+6K_s/d$, where d is the average particle size. The bulk anisotropy of ferrites is proportional to the Fe^{3+} ion concentration, which decreases in our samples as the Mg-Ti concentration rises. Assuming that surface anisotropies of all samples are the same, since they are prepared in the same conditions, K_{eff} decreases with increasing Mg-Ti amount. Therefore, we can expect a decrease in the coercive field as well, as depicted in Fig. 6 and in Table 3.

3.5. Electrical properties

It is important to understand electrical properties of any conductive NPs as a function of temperature and frequency. Subsequently, variation of the complex impedance can be evaluated with the help of Fourier Transform using the response signal to a sinusoidal stimulus. In this concept, the complex dielectric constant and conductivity can be calculated using equations $\varepsilon^*(\omega, T)=\varepsilon'(\omega, T)-i\,\varepsilon''(\omega, T)$ and $\sigma^*(\omega, T)=\sigma'(\omega, T)-i\,\sigma''(\omega, T)$, respectively.

It is prominent to note that the real part of the ac conductivity could be derived from the imaginary component of the dielectric constant $\varepsilon''(\omega)$ through the relation $\sigma'(\omega)=\varepsilon_0\omega\varepsilon''(\omega)$ for each frequency value, where ε_0 is the vacuum permittivity, and $\omega=2\pi f$ is the angular frequency. In this study, ac conductivity of the Mg-Ti substituted Ni-Zn spinel ferrites [$Ni_{0.5}Zn_{0.5}Mg_xTi_xFe_{2-2x}O_4$ (where $0.05 \le x \le 0.25$)] was derived at temperatures from 20 up to 120 °C using standard impedance spectroscopy. The frequency dependent conductivities of all the ferrites studied were obtained through the standard equation as follows [43,44]; $\sigma'(\omega, T) = \varepsilon''(\omega, T)\omega(T)\varepsilon_0$, where $\sigma'(=\sigma_{ac}(\omega, T)$ is the real component of complex conductivity, ε'' is the imaginary component of complex dielectric permittivity (ε^*), ε_0 ($=8.852\times10^{-14}$ F/cm) is the vacuum permittivity, and finally, ω is the angular frequency of the electric field applied across the electrodes. The frequency dependency of the real part of the conductivity follows a power law behavior in some region, while it remains constant at lower frequencies. Besides, it changes with Mg-Ti concentration. In general, the total conductivity could be represented by the following equation:

$$\sigma'(\omega, T) = \sigma_{dc} + \sigma(T)\omega^n \quad (1)$$

where σ_{dc} is the frequency-independent component of conductivity or dc conductivity (at $\omega\to0$), $\sigma(T)$ is the temperature-dependent coefficient, and "n" is a power exponent around unity

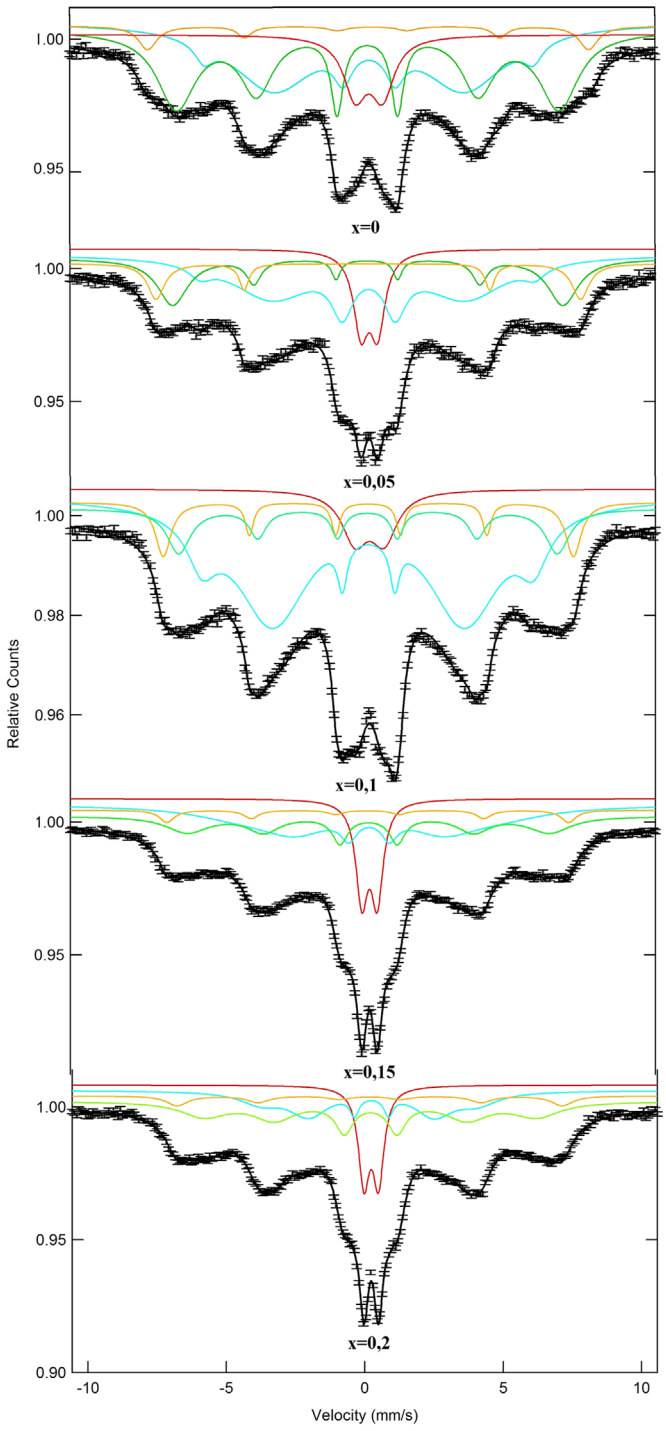

Fig. 3. Room temperature Mössbauer spectra of $Ni_{0.5}Zn_{0.5}Mg_xTi_xFe_{2-2x}O_4$ NPs.

which depends on both frequency and temperature. The conductivity at the lowest frequency, 1 Hz, was taken as dc part, σ' (1 Hz, T) = σ_{dc} (T). This type of electrical behavior can be attributed to the theory of universal dynamic response proposed by Macdonald [45].

It should be noted that measuring the frequency dependent conductivity is an informative method to understand both type and mechanisms of the transport properties of ferrites. In general, the conductivity in ferrites has two components, namely dc and ac conductivity. The mechanism of the former one is the band conduction [46] and that of the latter one is hopping between ions of the same element having more than one valence state, which can be expressed by the power law.

3.5.1. *ac conductivity*

The ac conductivity curves of Mg-Ti substituted Ni-Zn NPs as a function of frequency up to 3 MHz and at temperatures ranging from 20 to 120 °C are shown in Fig. 7. It can be noticed that ac conductivities of all Mg-Ti-substituted Ni-Zn spinel ferrites vary in a range between 30 nS/cm and 500 μS/cm as the temperature and frequency changes within the ranges mentioned above. The amount of Mg-Ti ions in Ni-Zn spinel ferrites affects the ac conductivity tremendously as can be easily seen in Fig. 7(a)–(e). It raises rather linearly with increasing temperature, while it decreases as Mg-Ti amount increases in the samples. In addition, at low frequencies, it becomes frequency independent for all temperatures and Mg-Ti concentrations. The ac conductivity stays almost constant, for example, up to 50 kHz when x = 0.05 as illustrated in Fig. 7(e). Therefore, we can expect that the frequency-independent conductivity can be extended to a higher frequency region when the temperature increases above 120 °C.

Furthermore, ac conductivity increases with temperature at low frequencies while it remains almost constant in the high frequency regime for various Mg-Ti substitution levels. Once substitution is increased, the ac conductivity becomes less temperature dependent [47]. The increase of conductivity at higher frequencies may be attributed to the predominance of the hopping type transition. This behavior can be considered as strong evidence for the ionic conductivity [48].

3.5.2. *dc conductivity*

The dc conductivity measurements of the Mg-Ti substituted Ni-Zn NPs are shown in Fig. 8 in an Arrhenius plot as a function of reciprocal temperature between 20 and 120 °C with an interval of 10 °C. Thus, the dc conductivity can be expressed by means of a well-known Arrhenius plot as;

$$\sigma_{dc}(T) = \sigma(0)\exp\left[-\frac{E_a}{k_B T}\right] \quad (2)$$

for a broad range of activation energies depending upon the amount of Mg-Ti substitution (where $k_B = 8{,}6173324 \times 10^{-5}$ eV/K). Activation energies of the samples have been calculated by fitting a linear curve and were determined to vary between 370–600 meV, see Table 4. It can be easily seen that for the highest Mg-Ti concentration, the activation energy does not follow the Arrhenius plot at low temperatures indicating a weak activation tendency.

The possibility to tune the activation energy by varying the Mg-Ti amount in Ni-Zn spinel ferrites is illustrated in Fig. 8(b), the maximum value of nearly 600 meV is achieved at about x = 0.16 while it decreases both ways down to 370 meV for $x < 0.05$ and also roughly above 0.30. Temperature-independent pre-coefficients of the conductivity, $\sigma(0)$, were found to be dependent only upon the Mg-Ti concentration in Ni-Zn spinel ferrites. So, the coefficients show a Gaussian variation having a peak value of 5,8 S/cm centered at x = 0.16 which corresponds to the maximum activation energy.

3.5.3. *Dielectric properties (ε' and ε'')*

Permittivity spectra of the Mg-Ti subsituted Ni-Zn NPs were obtained by plotting dielectric constants ε' and ε'' as a function frequency up to 3 MHz at various temperatures ranging from 20 to 120 °C. It is clearly seen from Fig. 9 that both magnitude and frequency dependence of ε' changes with the Mg-Ti concentration. It was observed in all prepared samples that the real part of the dielectric constant ε' decreases with increasing frequency at all temperatures. The orientational polarization decreases with

Table 2
Parameters of Mössbauer Spectra of the $Ni_{0.5}Zn_{0.5}Mg_xTi_xFe_{2-2x}O_4$ NPs (B_{hf}: hyperfine magnetic field. I.S: isomer shift. Q.S: quadrupole splitting. W: line width. R_A: Relative area).

Mg-Ti concentration, x	Assignment of sites	I.S . ($\pm$0.01) (mm s^{-1})	Q.S. ($\pm$0.02) (mm s^{-1})	B_{hf} ($\pm$0.2) (T)	W ($\pm$0.01) (mm s^{-1})	R_A (%)
0	Sx- A: Fe^{+3}	0.2936	0.0147	42.852	0.5472	31.305
	Sx- B: Fe^{+3}	0.3919	−0.1488	49.38	0.8081	5.2465
	Sx- B_1: Fe^{+3}	0.3414	−0.0119	36.852	0.8146	50.21
	Db: Fe^{+3}	0.3436	0.9881	–	1.011	13.238
0.05	Sx- A: Fe^{+3}	0.2781	0.0347	43.716	0.3816	11.669
	Sx- B: Fe^{+3}	0.2884	0.0483	47.548	0.4161	5.6282
	Sx- B_1: Fe^{+3}	0.3083	−0.0398	36.979	0.8023	70.642
	Db: Fe^{+3}	0.3457	0.5994	–	0.6533	12.061
0.1	Sx- A: Fe^{+3}	0.2819	0.0237	42.41	0.5395	13.499
	Sx- B: Fe^{+3}	0.2976	0.0063	45.938	0.3564	6.493
	Sx- B_1: Fe^{+3}	0.2952	−0.0285	37.127	0.4202	60.71
	Db: Fe^{+3}	0.3465	1.0559	–	1.1433	19.298
0.15	Sx- A: Fe^{+3}	0.3111	−0.0041	40.584	0.6735	26.617
	Sx- B: Fe^{+3}	0.2788	0.0070	44.997	0.619	5.351
	Sx- B_1: Fe^{+3}	0.3511	0.0317	28.686	0.7029	52.92
	Db: Fe^{+3}	0.3366	0.5917	–	0.5495	17.975
0.2	Sx- A: Fe^{+3}	0.3159	−0.0079	37.283	0.7696	50.2
	Sx- B: Fe^{+3}	0.2856	0.0019	43.165	0.8887	12.079
	Sx- B_1: Fe^{+3}	0.31	−0.0799	24.026	0.4020	21.2
	Db: Fe^{+3}	0.3381	0.5233	–	0.4808	16.521

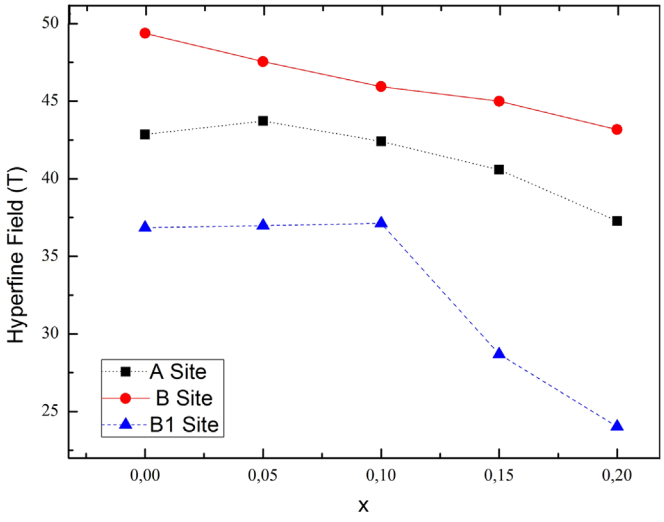

Fig. 4. Variation of hyperfine magnetic field at the A-, B- and B_1- sites with x in $Ni_{0.5}Zn_{0.5}Mg_xTi_xFe_{2-2x}O_4$NPs.

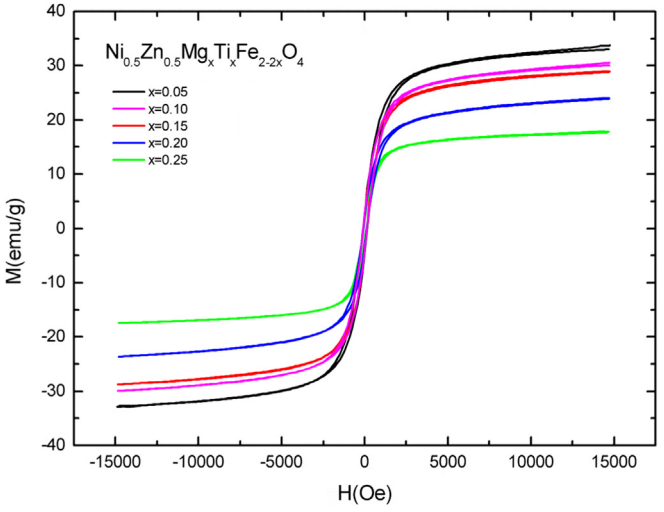

Fig. 5. Magnetic hysterisis curves of $Ni_{0.5}Zn_{0.5}Mg_xTi_xFe_{2-2x}O_4$ ($0.05 \le x \le 0.25$) NPs.

Table 3
Magnetic parameters of $Ni_{0.5}Zn_{0.5}Mg_xTi_xFe_{2-2x}O_4$ ($0.05 \le x \le 0.25$) NPs.

Amount of substitution (x)	Ms (emu/g)	Mr (emu/g)	Hc (Oe)
0.05	34.3	2.9	126
0.10	30.6	2.9	118
0.15	18.5	2.5	108
0.20	25.6	2.4	104
0.25	18.3	1.4	86

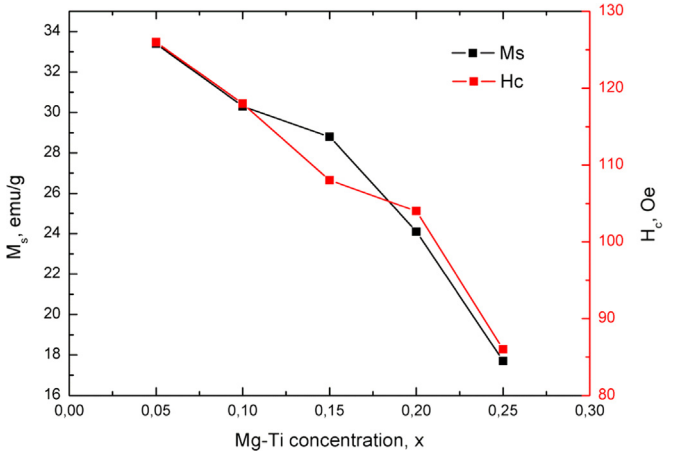

Fig. 6. Coercivity and saturation magnetization values of Ni-Zn ferrite NPs for different Mg-Ti concentrations.

increasing frequency since the dipole moments require long time to follow the oscillations of the alternating field. Thus, dielectric constant decreases. It is also common for all substitution levels that as the temperature raises the dielectric constant ε′ increases, which was clearly observed at low frequencies when Mg-Ti concentration is high (i.e., x=0.25) and at high frequencies for low Mg-Ti amounts (i.e., x=0.05 and 0.10). This can be explained by an increase in the molecular orientation and re-arrangement with temperature [49]. Besides, it is clearly seen that the temperature dependency shifts to higher frequencies as the Mg-Ti concentration decreases.

The imaginary component of the permittivity ε″ spectra of Mg-Ti substituted Ni-Zn NPs is shown as log-log plots in Fig. 10 for the

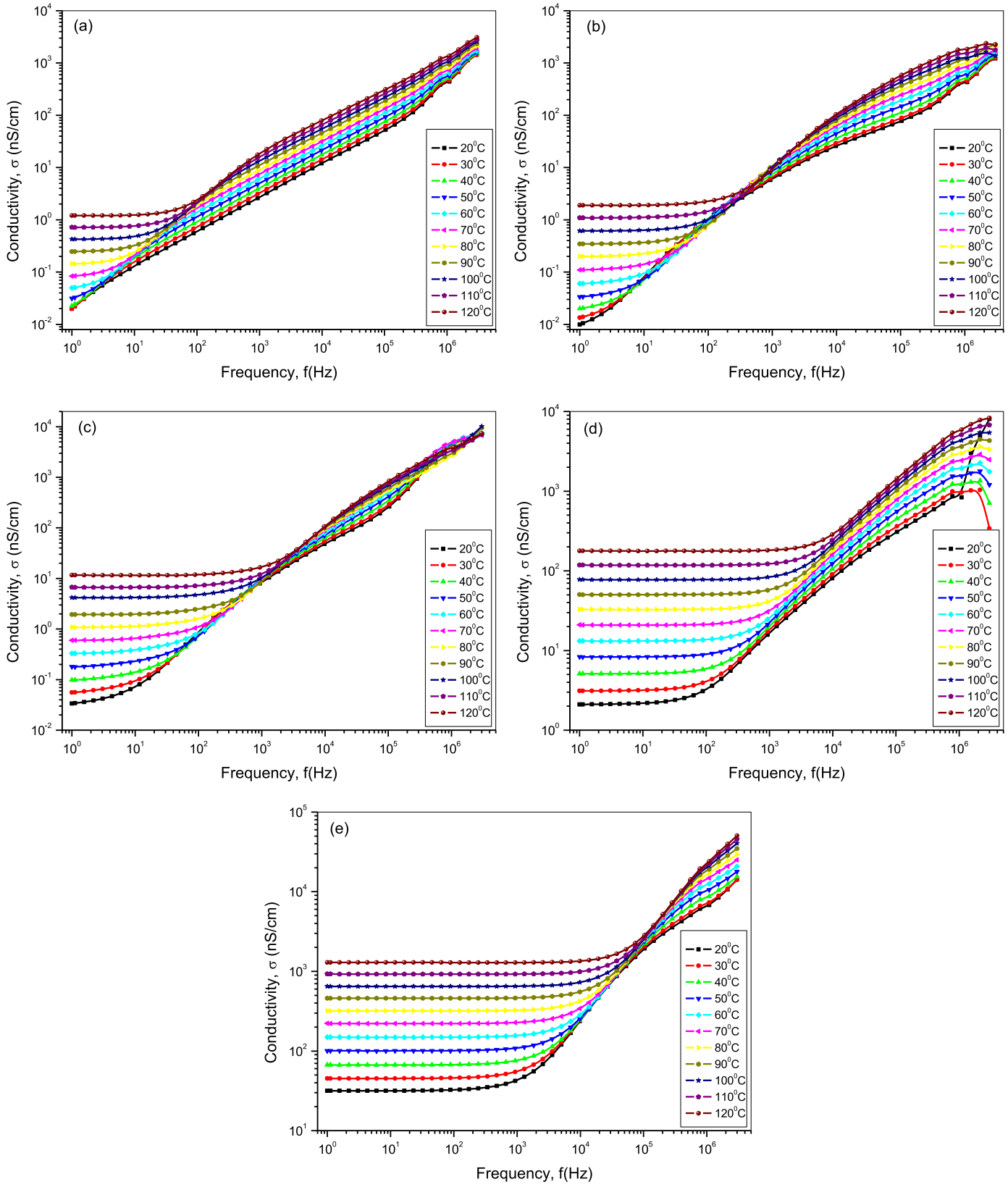

Fig. 7. ac conductivities of MgTi-substituted Ni-Zn spinel ferrites NPs, $[Ni_{0.5}Zn_{0.5}Mg_xTi_xFe_{2-2x}O_4]$ (a) x=0,25; (b) x=0,20; (c) x=0,15; (d) x=0,10; (e) x=0,05 as a function of frequency up to 3 MHz for temperature ranging from 20 to 120 °C.

same temperature interval. It was observed that ε″ is strongly temperature dependent at low frequencies and at high Mg-Ti concentrations. As the Mg-Ti amount decreases, the temperature dependent regime extends up to frequencies above 10 kHz.

The dielectric loss ε″ can clearly be expressed as a power law $\varepsilon''(\omega, T)=\varepsilon''(0,T)\omega^{-n}$, where $\varepsilon''(0,T)$ is a temperature dependent coefficient. It can be realized that the power exponent "n" of almost each curve is close to unity for all temperatures and for all

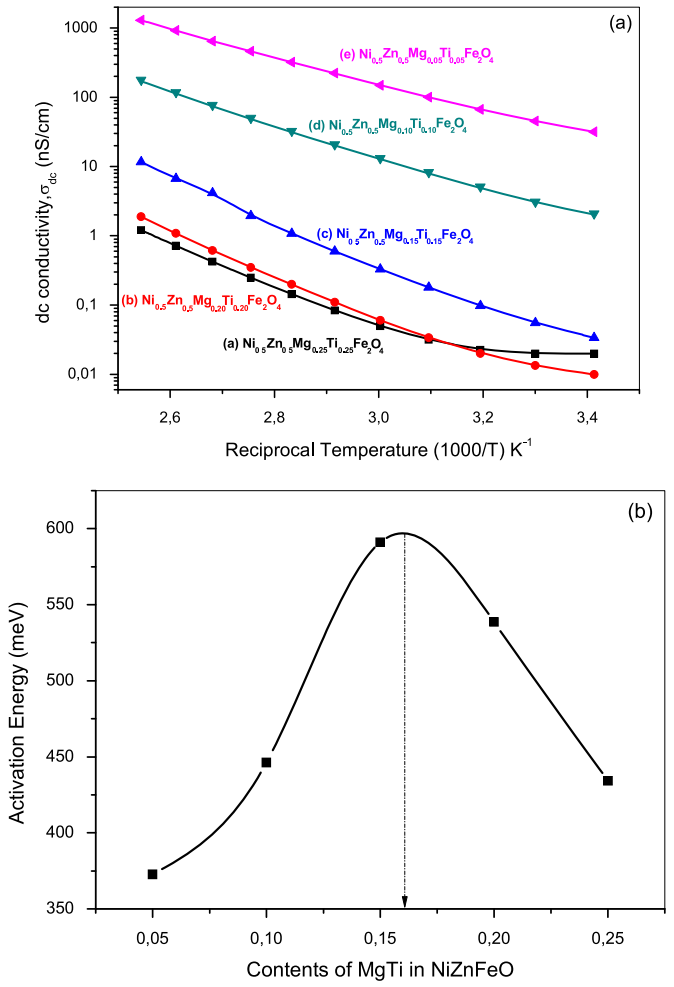

Fig. 8. (a) Arrhenius plots of dc electrical conductivities of $Ni_{0.5}Zn_{0.5}Mg_xTi_xFe_{2-2x}O_4$ (where $0.05 \le x \le 0.25$) NPs as a function of reciprocal temperature ranging from 20 to 120 °C. (b) Variation of activation energy as a function of Mg-Ti content in $Mg_xTi_xNi_{0.5}Zn_{0.5}Fe_2O_4$ NPs centered at x=0.16.

Table 4
Variations of each activation energy of Mg-Ti substituted Ni-Zn spinel ferrites [$Ni_{0.5}Zn_{0.5}Mg_xTi_xFe_{2-2x}O_4$ (where $0.05 \le x \le 0.25$)].

Compositions	Activation energy (meV)
$Ni_{0.5}Zn_{0.5}Mg_{0.05}Ti_{0.05}Fe_{1.9}O_4$	373
$Ni_{0.5}Zn_{0.5}Mg_{0.10}Ti_{0.10}Fe_{1.8}O_4$	446
$Ni_{0.5}Zn_{0.5}Mg_{0.15}Ti_{0.15}Fe_{1.7}O_4$	591
$Ni_{0.5}Zn_{0.5}Mg_{0.20}Ti_{0.20}Fe_{1.6}O_4$	538
$Ni_{0.5}Zn_{0.5}Mg_{0.25}Ti_{0.25}Fe_{1.5}O_4$	434

Mg-Ti amounts. This observation is similar to the tendencies detected in $NiFe_2O_4$, and $CoFe_2O_4$ and Mn-substituted Ni-Zn spinel ferrites [50,51].

The dielectric loss increases when temperature rises up to 120 °C at low frequencies. However, the effect of temperature is less significant at high frequencies, as expected, and can be explained by the Maxwell-Wagner model of inhomogenous double structure [52,53]. According to the model, the highly conducting grains are separated by poor conducting grain boundaries, which leads to accumulation of charge carries at the boundaries. Therefore, more energy is required for polarization within the grain boundaries at low frequencies, which leads to the high energy loss. On the other hand, relatively low energy is need for polarization in the grains which results in low energy losses at high frequencies [54,55].

3.5.4. Dielectric complex modulus

The complex dielectric modulus can be derived from both real and imaginary components of complex dielectric data (ε' and ε''), and then is expressed as:

$$M^* = \frac{1}{\varepsilon^*} = M' + iM'' = \frac{\varepsilon' + i\varepsilon''}{\varepsilon'^2 + \varepsilon''^2} \quad (3)$$

where M′and M′′ are the real and complex components of the dielectric modulus, respectively.

Dependences of the real part of the complex dielectric modulus on the applied signal frequency for a variety of Mg-Ti substituted Ni-Zn spinel ferrites at temperatures up to 120 °C with an increment of 10 °C are summarized in Fig. 11. It is evident that the real part of the dielectric modulus decreases with temperature at low frequencies for all Mg-Ti substitution levels between 0.25 and 0.05, while there is a saturation at frequencies above 40 Hz for x=0.25 and above 20 kHz for x=0.05.

It can be clearly stated that the real part of the modulus is shifted to the higher frequency side for all the samples as the temperature is increased from room temperature up to 120 °C. Moreover, the saturation region for each curve is also shifted. Thus, the real modulus can be expressed as a power law as: [56] $M'(\omega, T) = M'(0,T)\omega^n$, with an almost linear change of "n" with frequency having a small temperature-dependent deviation at the low frequency region at all temperatures and substitution levels. The linearity in the log-log plot of the real modulus is expanded into the higher frequency region as the temperature is increased from room temperature up to 120 °C, which is clearly evident in samples with a low concentration of Mg-Ti ions presented in Fig. 11(d and e).

The imaginary parts of the complex dielectric modulus, M′′, of the Mg-Ti substituted Ni-Zn NPs were measured at various temperatures ranging from 20 to 120 °C and are shown in Fig. 12. The linear character of the log-log plots is indicative of a power law behavior with the power exponent of approximately unity for low substitution levels, while for the higher substitutions (i.e. x=0.20 and 0.25) the plots exhibit some fluctuations in the whole frequency range. The imaginary modulus depends on the power exponent of the frequency according to the equation: $M''(\omega, T) = M''(0,T)\omega^n$, where $M''(0,T)$ is the pre-coefficient of the imaginary component of the complex dielectric modulus and "n" is the slope of the curves which is strongly temperature-dependent in the whole frequency range for low Mg-Ti amounts. Besides, the linearity of each curve is expanded to higher temperatures and higher frequencies as the Mg-Ti concentration decreases.

3.6. Microwave absorption properties

The reflection loss (RL) spectra of the synthesized samples were calculated according to the transmission line theory which states that the RL of a material backed by perfect conductor and illuminated by a wave with normal incidence can be derived as [57]:

$$RL(dB) = -20log\left|(Z_{in} - Z_0)/(Z_{in} + Z_0)\right| \quad (4)$$

where $Z_{in} = Z_0\sqrt{\mu_r/\varepsilon_r}\tanh\left[\left(-j\frac{2\pi fd}{c}\right)\sqrt{\mu_r\varepsilon_r}\right]$, $\mu_r = \mu' - j\mu''$ and $\varepsilon_r = \varepsilon' - j\varepsilon''$. Z_0 is the impedance of free space, f is the frequency and d is the thickness of the absorber. Z_{in} is the input impedance of an absorber which depends mainly on complex permittivity and permability values, which are derived from the reflection and transmission coefficients (i.e., S_{11} and S_{12}) using NRW algorithm [58]. Thus, Eq. (4) implies that the impedance matching condition

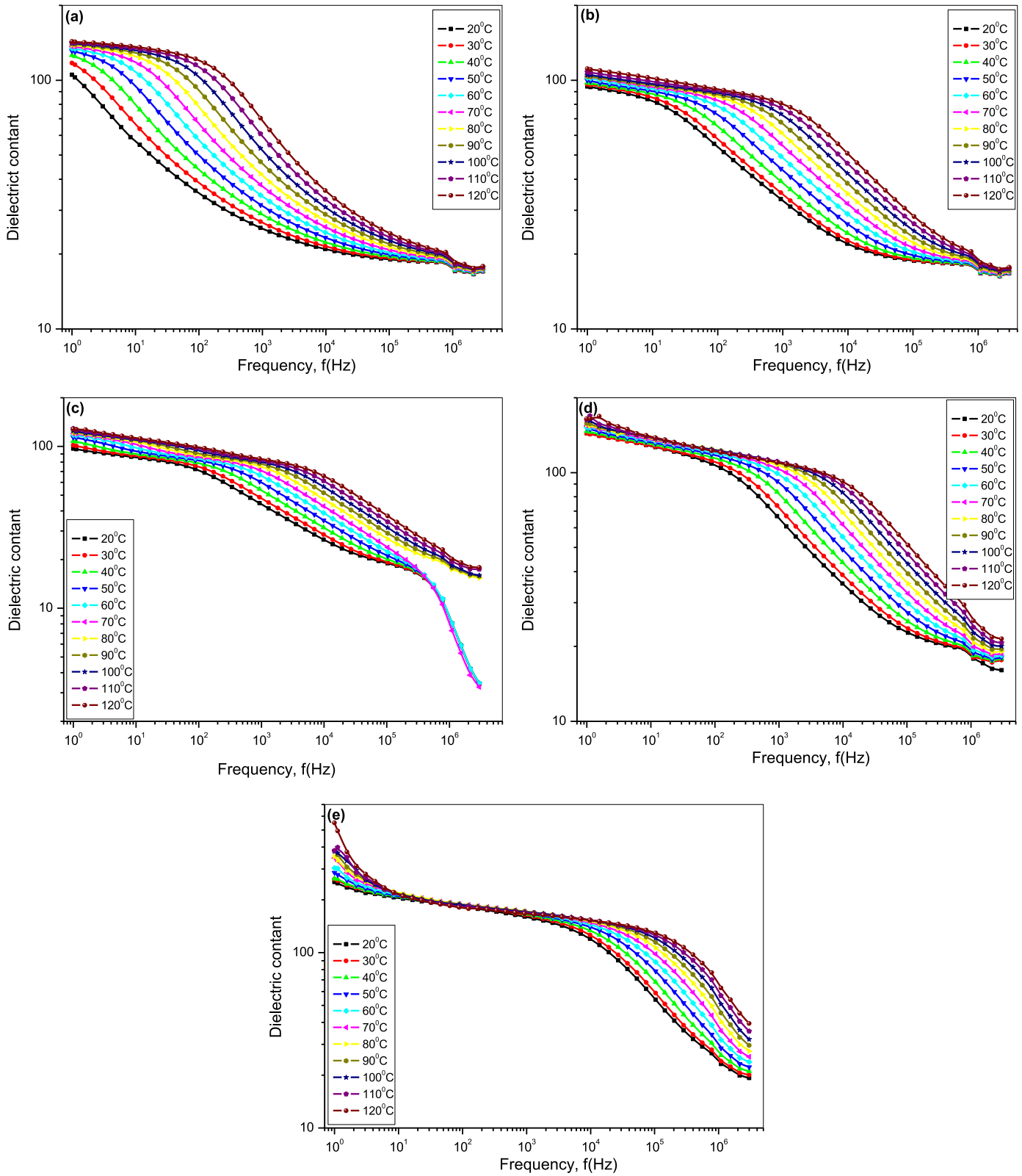

Fig. 9. Dielectric constant of MgTi-substituted Ni-Zn spinel ferrite [$Ni_{0.5}Zn_{0.5}Mg_xTi_xFe_{2-2x}O_4$] NPs (a) x=0,25; (b) x=0,20; (c) x=0,15; (d) x=0,10; (e) x=0,05 as a function of frequency up to 3 MHz for temperature ranging from 20 to 120 °C.

is satisfied when Z_{in} is equal to Z_0 (i.e. 377 Ω). Fig. 13 depicts the RL spectra of Mg-Ti substituted Ni-Zn ferrite NPs between 2 and 18 GHz. It shows that the minimum RL of nearly −30 dB@10 GHz occurs in samples having a Mg-Ti concentration of x=0.20 and 0.25, while the bandwidth of this absorption at −20 dB is 2 GHz. In addition, the samples having higher saturation magnetization values have weak RL properties of around −25 dB at the same frequency, see Table 5. The mechanism of absorption was determined as the quarter wave cancellation at the matching thickness. When electromagnetic wave is incident on an absorber

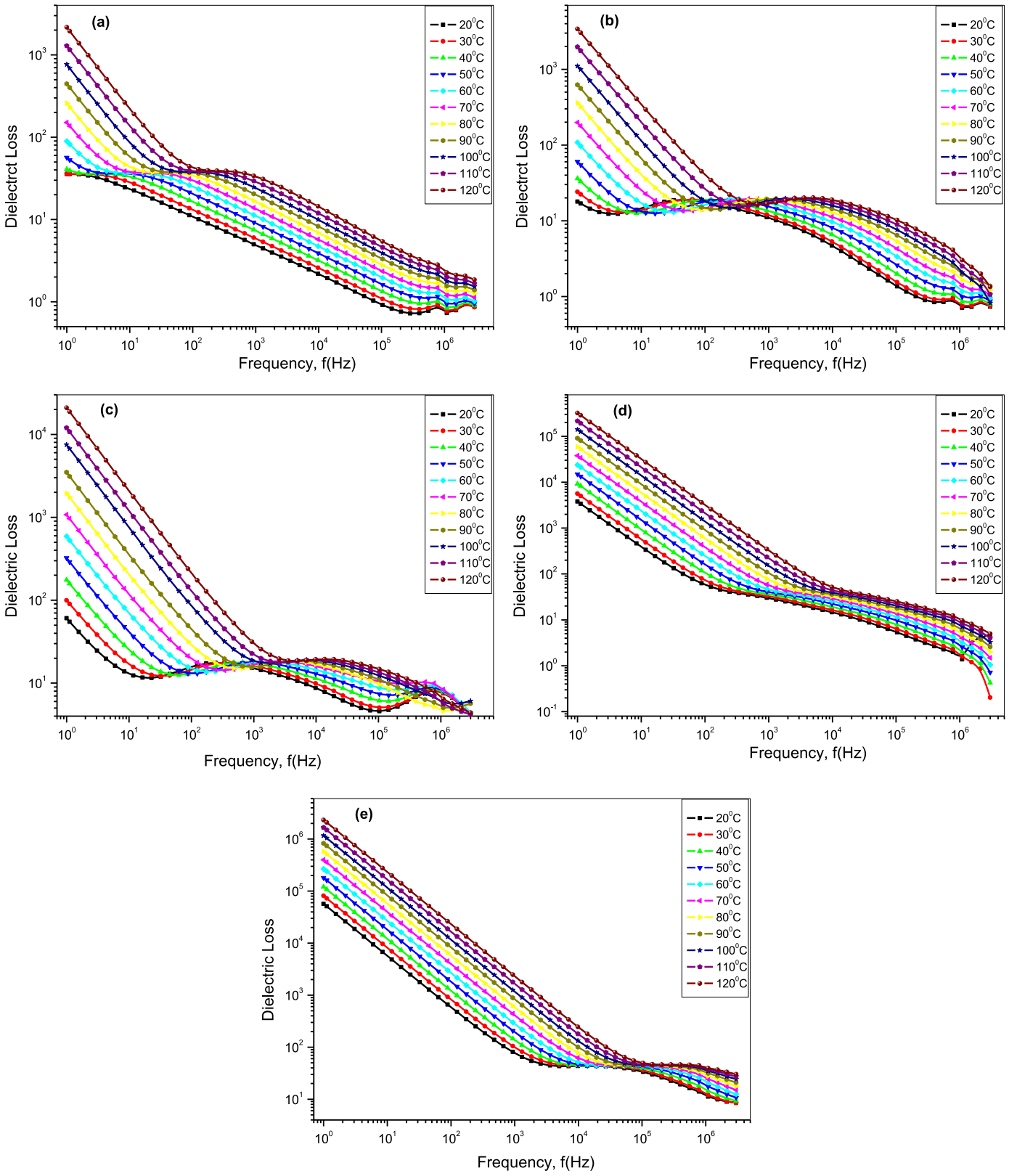

Fig. 10. Dielectric loss of Mg-Ti substituted Ni-Zn spinel ferrite [$Ni_{0.5}Zn_{0.5}Mg_xTi_xFe_{2-2x}O_4$] NPs (a) x=0,25; (b) x=0,20; (c) x=0,15; (d) x=0,10; (e) x=0,05 as a function of frequency up to 3 MHz for temperature ranging from 20 to 120 °C.

backed by a conductive metal plate, in some circumstances, the wave reflected at the air-absorber interface is 180° out of phase with the wave reflected at the absorber–metal interface canceling each other at the air-absorber interface. If the thickness of an absorber is equal to one quarter of the wavelength, this cancellation occurs at the matching thickness, t_m. Similarly, the frequency at which RL occurs is referred to as the matching frequency, f_m [59]. The relation between the matching thickness and the

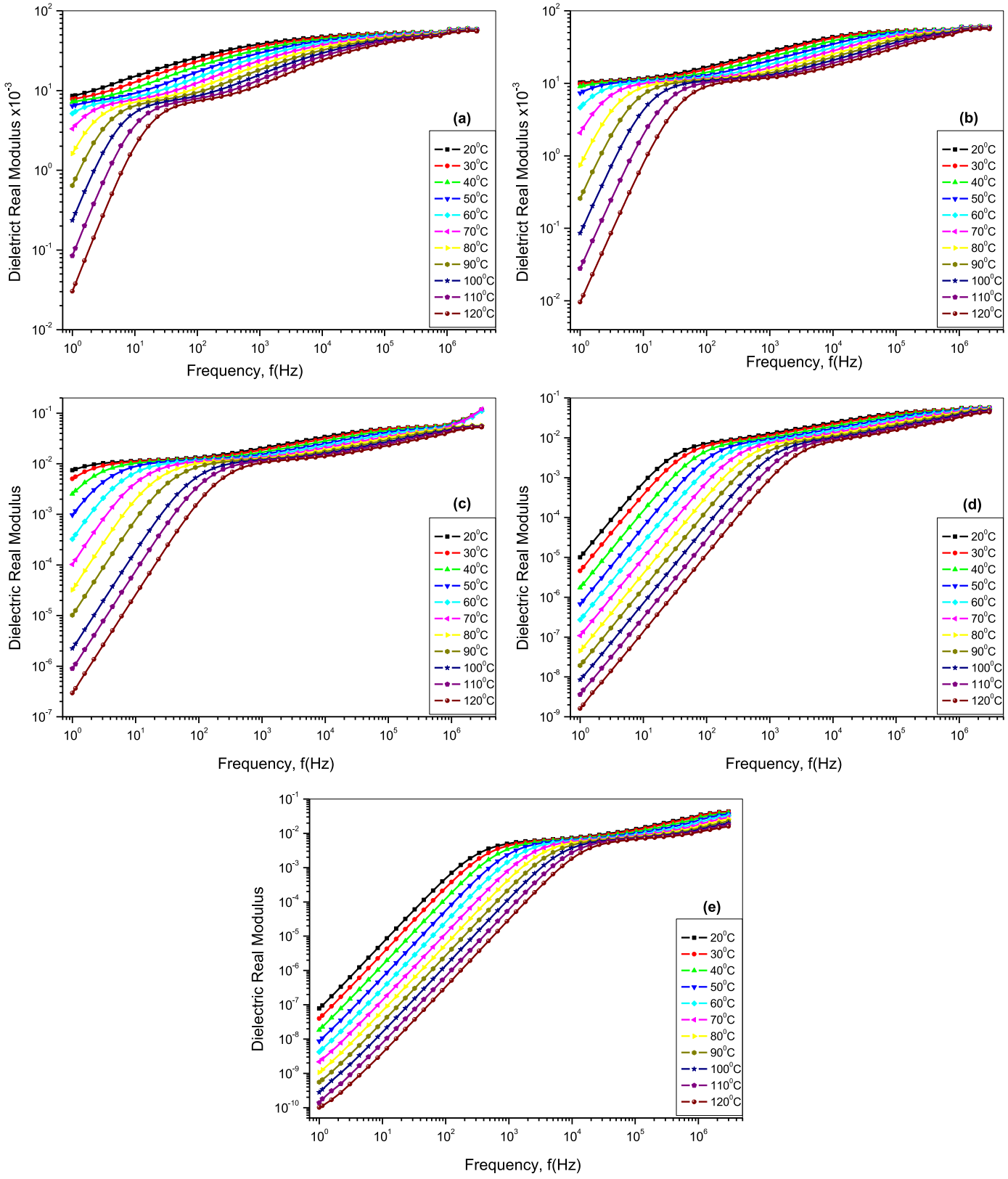

Fig. 11. Real part of complex dielectric modulus of Mg-Ti substituted Ni-Zn spinel ferrite [$Ni_{0.5}Zn_{0.5}Mg_xTi_xFe_{2-2x}O_4$] NPs (a) x=0,25; (b) x=0,20; (c) x=0,15; (d) x=0,10; (e) x=0,05 as a function of frequency up to 3 MHz for temperature ranging from 20 to 120 °C.

matching frequency is:

$$t_m = \frac{n\lambda}{4} = \frac{nc}{4f\sqrt{|\varepsilon_r||\mu_r|}} (\text{n=1, 3, 5. . }) \quad (5)$$

This equation shows that when the thickness of an absorber is equal to one quarter of the wavelength, the quarter-wave thickness criteria is satisfied. Fig. 14 shows the matching thickness spectra of our 3 mm thick samples up to 18 GHz. As seen in the

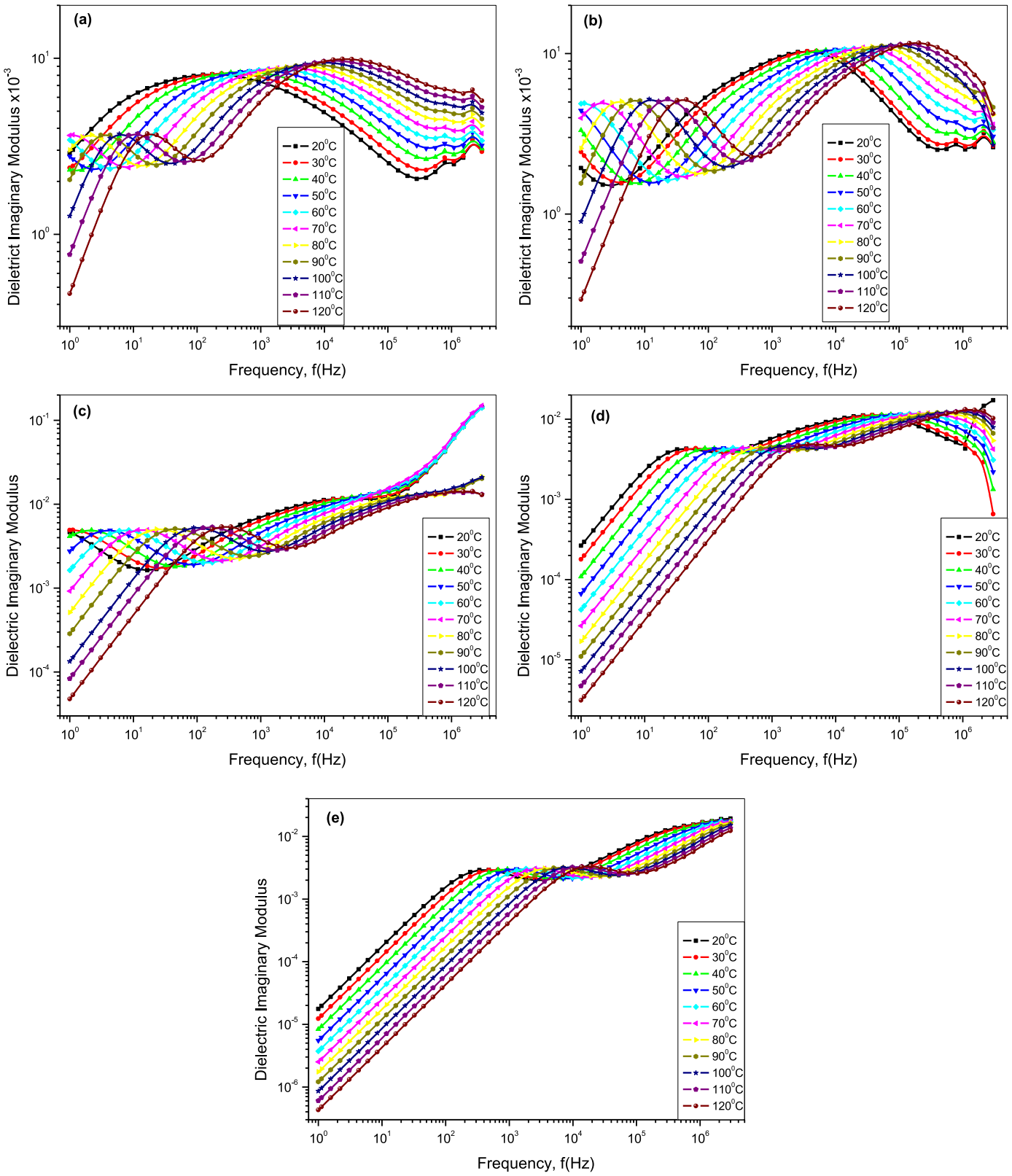

Fig. 12. Imaginary part of complex dielectric modulus of Mg-Ti substituted Ni-Zn spinel ferrite [$Ni_{0.5}Zn_{0.5}Mg_xTi_xFe_{2-2x}O_4$] NPs (a) x=0,25; (b) x=0,20; (c) x=0,15; (d) x=0,10; (e) x=0,05 as a function of frequency up to 3 MHz for temperature ranging from 20 to 120 °C.

figures, the matching thickness becomes equal to the thicknesses of absorbers exactly at the same frequencies where RL occurs in Fig. 13 indicating that the mechanism of absorption is the quarter wave cancellation.

The RL spectra of the sample having the best microwave absorption ($Ni_{0.5}Zn_{0.5}Mg_{0.25}Ti_{0.25}Fe_{1.5}O_4$) have been calculated for various thicknesses between 2 and 10 mm and are shown in Fig. 15. It should be noticed that as sample thickness increases the

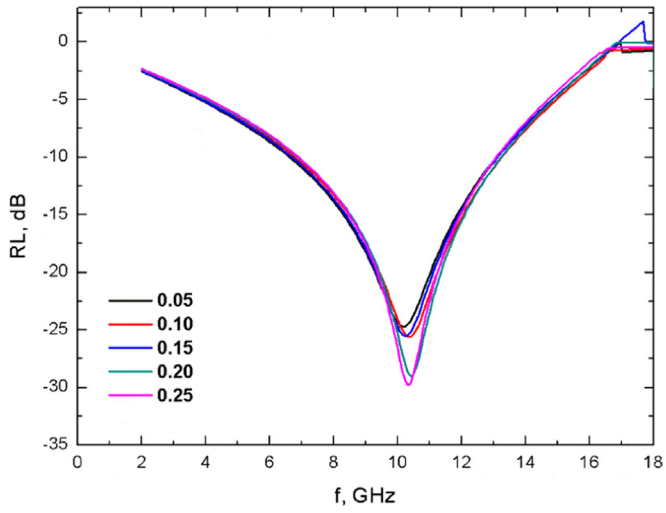

Fig. 13. RL values of $Ni_{0.5}Zn_{0.5}Mg_xTi_xFe_{2-2x}O_4$ ($0.05 \le x \le 0.25$) NPs in 2–18 GHz range.

Table 5
Microwave properties of $Ni_{0.5}Zn_{0.5}Mg_xTi_xFe_{2-2x}O_4$ ($0.05 \le x \le 0.25$) samples in 2–18 GHz range.

	Frequency (GHz)	RL (dB)
$Ni_{0.5}Zn_{0.5}Mg_{0.05}Ti_{0.05}Fe_{1.90}O_4$	10.16	−24.73
$Ni_{0.5}Zn_{0.5}Mg_{0.10}Ti_{0.10}Fe_{1.8}O_4$	10.4	−25.6
$Ni_{0.5}Zn_{0.5}Mg_{0.15}Ti_{0.15}Fe_{1.7}O_4$	10.32	−25.45
$Ni_{0.5}Zn_{0.5}Mg_{0.20}Ti_{0.20}Fe_{1.6}O_4$	10.48	−28.94
$Ni_{0.5}Zn_{0.5}Mg_{0.25}Ti_{0.25}Fe_{1.5}O_4$	10.32	−29.76

matching frequency of the absorber decreases. Thus, the thinner the absorber the higher its matching frequency. The 2 mm thick sample has a RL of −37 dB@16 GHz, while it is −25 dB@3 GHz for the thickness of 10 mm. In Fig. 16, matching thickness values are plotted as a function of matching frequencies for the sample thicknesses between 2 and 10 mm. It was observed that as sample thickness increases the matching frequency of the absorber decreases exponentially. The solid line in Fig. 16 corresponds to the exponentially fitted curve of the first order which agrees well with the experimental data. The same behavior was also observed and reported in our previous works on both hexa- [5] and spinel ferrite absorbers [60].

4. Conclusion

$Ni_{0.5}Zn_{0.5}Mg_xTi_xFe_{2-2x}O_4$ ($0.05 \le x \le 0.25$) spinel ferrites have been synthesized using the conventional solid state reaction method with 1 wt% B_2O_3 addition. XRD and SEM characterizations show that single phase Ni-Zn spinel ferrites have been obtained with inhomogenous grain size distribution around 1–2 μm. The Mössbauer spectra of the prepared samples have ferromagnetic sextets and paramagnetic doublet for the samples. Besides, the hyperfine field values at B-, B_1- and A- sites gradually decrease with increasing concentration of Mg^{2+} and Ti^{4+} ions (x). The cubic symmetry of the crystal lattice was not influenced by substituted ions, both of which prefer to occupy octahedral sites (B-sites). Magnetic measurements revealed that the magnetization of the samples decreases as the Mg-Ti concentration increases, which was explained by the site preferences of the subsituted ions that lead to weak superexchange interactions. Electrical and dielectric characterization of Mg-Ti substituted Ni-Zn spinel ferrites showed that there are significant changes in both ac and dc conductivity, as

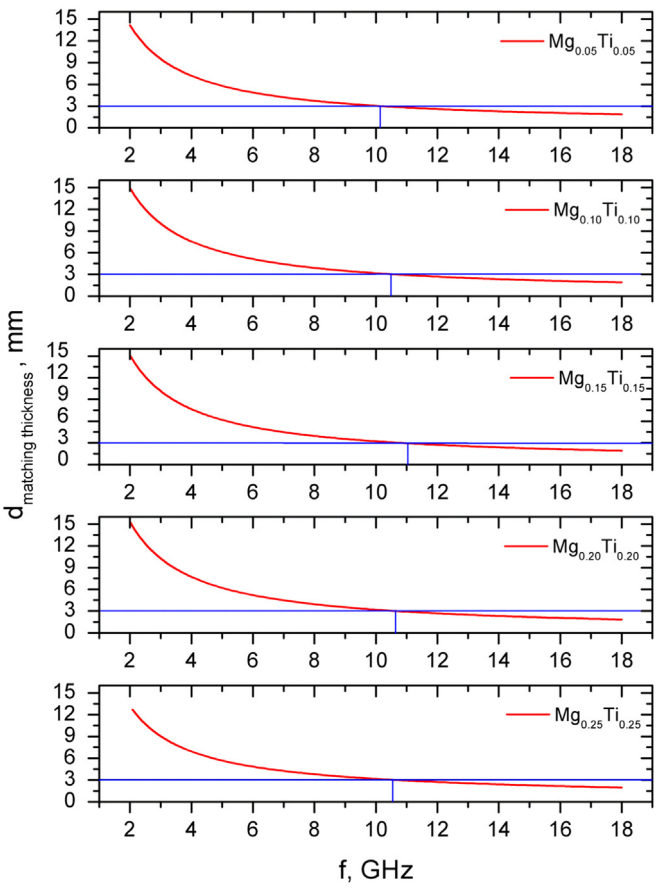

Fig. 14. Matching thickness curves of Ni-Zn ferrite samples having different Mg-Ti concentrations.

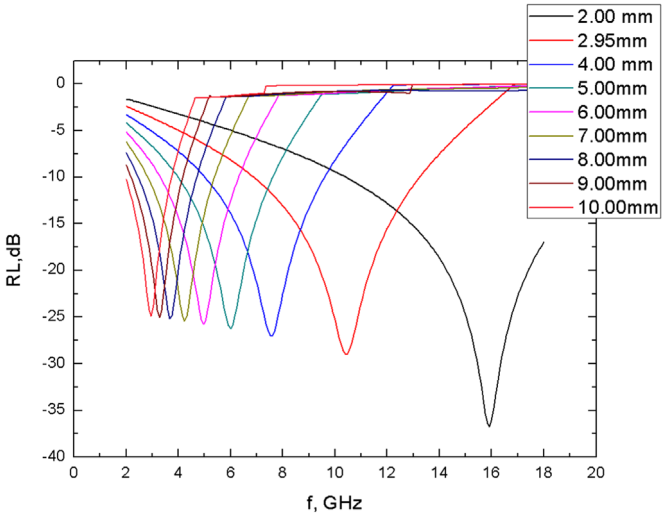

Fig. 15. RL spectra of $Ni_{0.5}Zn_{0.5}Mg_{0.25}Ti_{0.25}Fe_{1.5}O_4$ NPs calculated up to 18 GHz for various thicknesses between 2 and 10 mm.

well as complex permittivity, when the concentration of the substituted ions varies between 0.05 and 0.25. Taking into account the exponential behavior of the conductivity, the rate constant can be assigned to an Arrhenius expression. Thus, this brings about a variety of activation energies for all the composition ratios. The maximum observed activation energy was about 0.16. Furthermore, both the dielectric loss and imaginary parts of the modulus are found to almost obey the power law with a fixed exponent value in some frequency region, especially for lower Mg-Ti

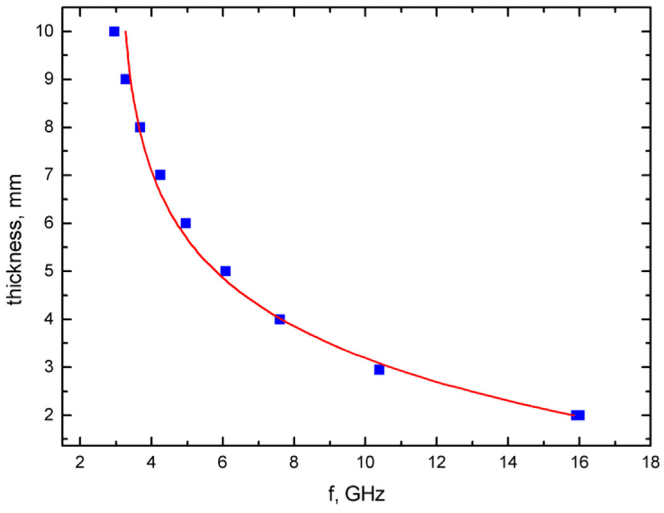

Fig. 16. Varion of matching thickness values of $Ni_{0.5}Zn_{0.5}Mg_{0.25}Ti_{0.25}Fe_{1.5}O_4$ NPs with frequency up to 18 GHz.

substitution levels. Both electrical properties and their complex dielectric behavior at low frequencies may be explained with the existence of a conventional tunneling conduction mechanism which depends on temperature, while being insensitive to the frequency. The microwave characterization showed that 3 mm thick samples have one reflection loss minimum around 10 GHz with varying magnitudes between −25 and −30 dB. The sample which has the highest Mg-Ti amount, $Ni_{0.5}Zn_{0.5}Mg_{0.25}Ti_{0.25}Fe_{1.5}O_4$, shows the best microwave properties in the 2–18 GHz frequency range. It has a reflection loss of higher than −35 dB at 16 GHz in the 2 mm thick specimen. It was also observed that the matching frequency of the Ni-Zn NPs decreases exponentially with increasing sample thickness. Finally, it can be concluded that the $Ni_{0.5}Zn_{0.5}Mg_{0.25}Ti_{0.25}Fe_{1.5}O_4$ NPs can be used as radar absorbing material in X (8–12 GHz) and Ku-(12–18 GHz) bands.

Acknowledgment

This work was supported by TUBITAK (The Scientific and Technological Research Council of Turkey) with Project number 213M174.

References

[1] J. Zhan, Y.L. Yao, C.F. Zhang, C.J. Li, Synthesis and microwave absorbing properties of quasione-dimensional mesoporous NiCo2O4 nanostructure, J. Alloy. Comp. 585 (2014) 240–244.
[2] W.L. Song, M.S. Cao, L.Z. Fan, M.M. Lu, Y. Li, C.Y. Wang, H.F. Ju, Highly ordered porous carbon/wax composites for effective electromagnetic attenuation and shielding, Carbon 77 (2014) 130–142.
[3] S.S. Kim, D.H. Han, S.B. Cho, Microwave absorbing Properties of sintered NI–Zn Ferrite, IEEE Trans. Magn. 30 (1994) 4554–4556.
[4] D.L. Zhao, Q. Lv, Z.M. Shen, Fabrication and microwave absorbing properties of Ni–Zn spinel ferrites, J. Alloy. Compd. 480 (2009) 634–638.
[5] H. Sözeri, Z. Mehmedi, H. Erdemi, A. Baykal, U. Topal, B. Aktaş, Microwave properties of $BaFe_{11}Mg_{0.25}X_{0.25}Ti_{0.5}O_{19}$ (X^{+2}=Cu, Mn, Zn, Ni and Co) nanoparticlesin 0–26.5 GHz range, Ceram. Int. 42 (2016) 2611–2625.
[6] M. Pardavi-Horvath, Microwave applications of soft ferrites, J. Magn. Magn. Mater. 215–216 (2000) 171–183.
[7] M. Jalaly, M.H. Enayati, P. Kameli, Effect of composition on structural and magnetic properties of nanocrystalline ball milled Ni1–xZnxFe2O4 ferrite, Physica B 405 (2010) 507–512.
[8] S. Sharma, K. Verma, U. Chaubey, Influence of Zn substitution on structural, microstructural and dielectric properties of nanocrystalline nickel ferrites, Mater. Sci. Eng. B 167 (2010) 187–192.
[9] G.S. Shahane, A. Kumar, M. Arora, et al., Synthesis and characterization of Ni–Zn ferrite nanoparticles, J. Magn. Magn. Mater. 322 (2010) 1015–1019.
[10] C. Upadhyay, D. Mishra, H.C. Verma, et al., Effect of preparation conditions on formation of nanophase Ni-Zn ferrites through hydrothermal technique, J. Magn. Magn. Mater. 260 (2003) 188–194.
[11] S.A. Morrison, C.L. Cahill, E.E. Carpenter, et al., Magnetic and structural properties of nickel zinc ferrite nanoparticles synthesized at room temperature, J. Appl. Phys. 95 (2004) 6392–6395.
[12] M. Atif, M. Nadeem, R. Grössinger, et al., Studies on the magnetic, magnetostrictive and electrical properties of sol-gel synthesized Zn doped nickel ferrite, J. Alloy. Compd. 509 (2011) 5720–5724.
[13] F. Genç, E. Turhan, H. Kavas, U. Topal, A. Baykal, H. Sözeri, Magnetic and microwave absorption properties of $Ni_xZn_{0.9-x}Mn_{0.1}Fe_2O_4$ prepared by boron addition, J. Supercond. Nov. Magn. 28 (3) (2015) 1047–1050.
[14] H. Sozeri, F. Genç, B. Ünal, A. Baykal, B. Aktas, Magnetic, electrical and microwave properties of Mn-Co substituted NixZn0.8−xFe2O4 nanoparticles, J. Alloy. Compd. 660 (2016) 324–335.
[15] C.-H. Peng, H.-W. Wang, S.-W. Kan, M.-Z. Shen, Y.-M. Wei, S.-Y. Chen, Microwave absorbing materials using Ag-NiZn ferrite core-shell nanopowders as fillers, J. Magn. Magn. Mater. 284 (1–3) (2004) 113–119.
[16] K.H. Wu, T.H. Ting, C.I. Liu, C.C. Yang, J.S. Hsu, Electromagnetic and microwave absorbing properties of Ni0.5Zn0.5Fe2O4/bamboo charcoal core-shell nanocomposites, Compos. Sci. Technol. 68 (1) (2008) 132–139.
[17] W. Chunyu, S. Xiangqian, S. Fuzhan, Z. Yongwei, W. Yingde, Double-layer microwave absorber based on nanocrystalline Zn0.5Ni0.5Fe2O4/α-Fe microfibers, Mater. Des. 35 (2012) 363–368.
[18] H. Xiaogu, Z. Jing, Lai Min, S. Tianyi, Preparation and microwave absorption mechanisms of the NiZn ferrite nanofibers, J. Alloy. Compd. 627 (2015) 367–373.
[19] Y.Q. Chu, B. Zhang, J. Xiang, Synthesis of nickel-based ferrite nanofibers and their static magnetic and microwave absorption properties, Adv. Mater. Res. 631–632 (2013) 429–433.
[20] B.K. Rai, L. Wang, S.R. Mishra, V.V. Nguyen, J.P. Liu, Synthesis and magnetic properties of hard-soft SrFe10Al2O19/NiZnFe2O4 ferrite nanocomposites, J. Nanosci. Nanotechnol. 14 (7) (2014) 5272–5277.
[21] G. Pozo López, S.P. Silvetti, S.E. Urreta, A.C. Carreras, Structure and magnetic properties of NiZn ferrite/SiO2 nanocomposites synthesized by ball milling, J. Alloy. Compd. 505 (2) (2010) 808–813.
[22] K. Shimba, K. Furuta, N. Morimoto, N. Tezuka, S. Sugimoto, Microwave absorption properties of polymer modified Ni-Zn ferrite nanoparticles, Mater. Trans. 52 (4) (2011) 740–745.
[23] C.-H. Peng, C.-C. Hwang, J. Wan, J.-S. Tsai, S.-Y. Chen, Microwave-absorbing characteristics for the composites of thermal-plastic polyurethane (TPU)-bonded NiZn-ferrites prepared by combustion synthesis method, Mater. Sci. Eng.: B 117 (1) (2005) 27–36.
[24] J.S. Ghodake, R.C. Kambale, T.J. Shinde, P.K. Maskar, S.S. Suryavanshi, Magnetic and microwave absorbing properties of Co^{2+} substituted nickel-zinc ferrites with the emphasis on initial permeability studies, J. Magn. Magn. Mater. 401 (2016) 938–942.
[25] Y. Liu, S.C. Wei, Y.J. Wang, H.L. Tian, H. Tong, B.S. Xu, Characterization of (Mg, La) substituted Ni-Zn spinel ferrite, Phys. Procedia 50 (2013) 43–47.
[26] H. Zhao, R. Ma, G. Zhang, X. Li, Influence of Nd doping on microwave absorbing properties of nanocrystalline Ni-Zn ferrites, Integr. Ferroelectr. 127 (1) (2011) 1–8.
[27] F. Gao, D.-L. Zhao, Z.-M. Shen, Preparation and microwave absorbing properties of Cu doped Ni-Zn spinel ferrites, Adv. Mater. Res. 105–106 (1) (2010) 293–296.
[28] M.M. Rashad, E.M. Elsayed, M.M. Moharam, et al., Structure and magnetic properties of NixZn1−xFe2O4 nanoparticles prepared through co-precipitation method, J. Alloy. Compd. 486 (2009) 759–767.
[29] Z. Mehmedi, H. Sözeri, U. Topal, A. Baykal, Effect of annealing temperature and boron addition on magnetic properties of hexaferrites synthesized by standard ceramic method, J. Supercond. Nov. Magn. 28 (4) (2015) 1395–1404.
[30] H. Sözeri, Effect of pelletization on magnetic properties of BaFe12O19, J. Alloy. Compd. 486 (1–2) (2009) 809–814.
[31] R.D. Shannon, Acta Cryst. A 32 (1976) 751–767.
[32] H.S.C. O'Neill, A. Navrotsky, Simple spinels; crystallographic parameters, cation radii, lattice energies, and cation distribution, Am. Miner. 68 (1983) 181–194.
[33] H. Ji, Z. Lan, Z. Xu, H. Zhang, G.J. Salamo, IEEE Trans. Magn. 49 (2013) 4277–4280.
[34] R. Kulkarni, H. Joshi, Solid State Commun. 53 (1985) 1005.
[35] H.M. Widatallah, F.A.S. Al-Mamari, N.A.M. Al-Saqri, A.M. Gismelseed, I.A. Al-Omari, T.M.H. Al-Shahumi, A.F. Alhaj, A.M. Abo El Ata, M.E. Elzain, Mössbauer and magnetic studies of Mg1+2xSbxFe2−3xO4 spinel ferrites, Mater. Chem. Phys. 140 (1) (2013) 97.
[36] M. Siddique, N.M. Butt, Effect of particle size on degree of inversion in ferrites investigated by Mössbauer spectroscopy, Physica B: Condens. Matter 405 (19) (2010) 4211–4215.
[37] S. Singhal, J. Singh, S.K. Barthwal, K. Chandra, Preparation and characterization of nanosize nickel-substituted cobalt ferrites (Co1−xNixFe2O4), J. Solid State Chem. 178 (10) (2005) 3183.
[38] R.J. Joseyphus, A. Narayanasamy, K. Shinoda, B. Jeyadevan, K. Tohji, Synthesis and magnetic properties of the size-controlled Mn–Zn ferrite nanoparticles by oxidation method, J. Phys. Chem. Solids 67 (7) (2006) 1510.
[39] Z. Lijun, Y. Hua, Y. Lianxiang, C. Yuming, Z. Xueping, F. Shouhua, Magnetic properties of re-substituted Ni–Mn ferrite nanocrystallites, J. Mater. Sci. 42 (2) (2007) 686.

[40] J.P. Hodges, S. Short, J.D. Jorgensen, X. Xiong, B. Dabrowski, S.M. Mini, C. W. Kimball, Evolution of oxygen-vacancy ordered crystal structures in the perovskite series SrnFenO3n − 1 (n=2, 4, 8, and ∞), and the relationship to electronic and magnetic properties, J. Solid State Chem. 151 (2) (2000) 190.
[41] A.M. Gismelseed, A.A. Yousif, Mössbauer study of chromium-substituted nickel ferrites, Physica B: Condens. Matter 370 (1–4) (2005) 215.
[42] L. Neel, Ann. Phys. 18 (1932) 5.
[43] Y.F. Shen, R.P. Zerger, R.N. Deguzman, S.I. Suib, L. Mccurdy, D.I. Potter, C. L. Oyoung, Science 260 (1993) 511.
[44] B. Unal, Z. Durmus, H. Kavas, A. Baykal, M.S. Toprak, Mater. Chem. Phys. 123 (2010) 184.
[45] J.R. Macdonald, Solid State Ion. 133 (2000) 79.
[46] A.M. Abo El Ata, M.K. El Nirma, S.M. Attia, D. El Kony, A.H. Al-Hammadi, Studies of AC electrical conductivity and initial magnetic permability of rare-earth substituted Li-Co ferrites, J. Magn. Magn. Mater. 297 (2006) 33.
[47] U. Kurtan, Y. Junejo, B. Unal, A. Baykal, J. Inorg. Organomet. Polym. 23 (2013) 1089.
[48] A. Baykal, N. Bıtrak, B. Ünal, H. Kavas, Z. Durmuş, Ş. Özden, M.S. Toprak, J. Alloy. Compd. 502 (2010) 199.
[49] M. Amir, B. Ünal, M. Geleri, H. Güngüneş, S.E. Shirsath, A. Baykal, Electrical properties and hyperfine interactions of boron doped Fe3O4 nanoparticles, Superlattices Microstruct. 88 (2015) 450–466.
[50] B. Ünal, A. Baykal, Effect of Zn substitution on electrical properties of nano-crystalline cobalt ferrite, J. Supercond. Nov. Magn. 27 (2014) 469–479.
[51] F. Genç, B. Ünal, A. Baykal, H. Sozeri, Electrical properties of Mn-doped NixZn0.9 − xFe2O4 particles, J. Supercond. Nov. Magn. 28 (2015) 1055–1064.
[52] J.C. Maxwell, A Treatise on Electricity and Magnetism, 2, Oxford University Press, Oxford, 1873.
[53] K.W. Wagner, Zur theorie der unvollkommenen dielektrika, Ann. Phys. 345 (1913) 817.
[54] H. Deligöz, A. Baykal, M. Şenel, H. Sözeri, E. Karaoglu, M.S. Toprak, Synth. Met. 162 (2012) 590.
[55] İ.M. Afandiyeva, İ. Dökme, Ş. Altındal, M.M. Bülbül, A. Tataroğlu, Microelectron. Eng. 85 (2008) 247.
[56] C.S. Zhang, L. Yang, J. Magn. Magn. Mater. 324 (2012) 1469.
[57] Y. Naito, K. Suetske, IEEE Trans. Microw. Theory Tech. 19 (1) (1971) 65–72.
[58] A.M. Nicolson, G.F. Ross, Measurement of intrinsic properties of materials by time domain techniques, IEEE Trans. Instrum. Meas. IM-19 (1970) 377–382.
[59] A.N. Yusoff, M.H. Abdullah, S.H. Ahmad, S.F. Jusoh, A.A. Mansor, S.A.A. Hamid, J. Appl. Phys. 92 (2002) 876.
[60] H. Sözeri, F. Genç, B, Ünal A. Baykal, B. Aktaş, Magnetic, electrical and microwave properties of Mn-Co substituted NixZn0.8 − xFe2O4 nanoparticles, J. Alloy. Compd. 660 (2016) 324–335.